Received: 11 July 2020 | Revised: 9 January 2021 | Accepted: 21 February 2021

DOI: 10.1002/fld.4972

RESEARCH ARTICLE

WILEY

Implementation of weighted essentially non-oscillatory scheme for unsteady and steady compressible flow in pressure-based algorithm

Mojtaba Balaj | **Mohammad Hassan Djavareshkian**

Department of Mechanical Engineering, Ferdowsi University of Mashhad, Mashhad, Iran

Correspondence
Mohammad Hassan Djavareshkian, Department of Mechanical Engineering, Ferdowsi University of Mashhad, Mashhad Iran.
Email: javareshkian@um.ac.ir

Abstract

A pressure-based semi-implicit procedure has been developed for the computation of compressible flows on a system with collocated finite volume formulations. The method includes the implementation of a high-order accurate weighted essentially non-oscillatory scheme within the pressure-based algorithm which employs an approximate Riemann solver for the computation of the cell face inviscid fluxes. The developed scheme is applied to the computation of unsteady compressible flow through a shock tube which experiences various Mach numbers, and the computations are compared with an analytical solution. The computations indicate that the developed procedure leads to sharp discontinuity representation without creation of spurious oscillations. Then, the developed numerical method is utilized to investigate unsteady two-dimensional flow for a lax configuration and the results are compared with the results of the similar scheme in the density-based algorithm. At the end, the investigation of steady compressible flows in bump and wedge channel is considered. The simulations show a considerable improvement over the existing pressure-based method. The investigations show that the developed method is suitable for studying compressible steady and unsteady flows.

KEYWORDS

pressure-based, Riemann solver, sharp discontinuity, weighted essentially non-oscillatory (WENO)

1 | INTRODUCTION

In recent decades, the numerical study of flows with discontinuities has always been of interest to many researchers. They have tried to develop a unified method for analyzing the flow in compressible and incompressible regimes.[1-22] The main objective is to capture all flow phenomena including sharp discontinuities, with a minimum number of grid cells. It is often challenging to develop shock-capturing methods. Many efforts have been performed to develop such methods. Part of these efforts have resulted in the development of a high-order accurate bounded schemes, remarkably the total variation diminishing (TVD),[14,15,23] weighted compact nonlinear scheme,[24] monotone advection upstream splitting method,[25,26] essentially non-oscillatory (ENO)[27] and weighted essentially non-oscillatory (WENO)[28-34] techniques. Although high-order TVD scheme generally presents oscillation-free shock profiles, it switches to the first-order accuracy

at discontinuities to bound the results. In practical applications, a uniform second-order bounded scheme is very desirable. To eliminate the local restrictions of the TVD scheme, the high-order accurate ENO scheme has been developed by Harten et al.[35-38] Instead of restricting the increase of total variations as in TVD, the ENO scheme permits the variations to increase only by an amount on the level of local truncation errors. In TVD and ENO schemes, a proper flux limiter shall be utilized to bound the results near discontinuities. In 1994, a WENO scheme was introduced by Liu et al.[39] In the ENO scheme, after considering some polynomials, the smoothest polynomial is selected using an appropriate flux limiter at the target cell boundary, while WENO uses a series of weighted coefficients of all these polynomials and considers them all in the prediction of the flux at the target cell boundary without the need for any flux limiter. One of the advantages of WENO scheme is that it operates intelligently and it does not require any adjustments to match the flow regime. Because of the benefits and accuracy of the scheme, the development of WENO has been studied by many researchers and various versions of this family have been introduced (JSWENO,[40] MWENO,[41] WENOZ,[42] WENO17,[43] WENOMZ,[44] HWENO[45]). The details of these studies are not in the scope of the present work. In most of these versions, weighted coefficients are different from others. Most of these high-resolution schemes along with a Riemann solver have been applied in a density-based algorithm[35-45] which is only suitable and applicable to highly compressible flows. The numerical simulations of the transonic and supersonic flows are commonly performed by density-based methods which solve the set of the nonlinear coupled systems of equations governing the flux of mass, momentum, and energy. Due to the form of coupled equations, it is complicated to solve them implicitly and it is best to solve the system of equations explicitly to control the computational costs. It should be noted that, using the explicit method, a series of restrictions such as time step restriction are entered into the calculations. Nevertheless, a pressure-based algorithm can offer the capability of handling compressible and incompressible flows in a unified manner without any of the limitations mentioned for the density-based algorithm. In the pressure-based algorithm the momentum and energy equations are considered in a segregated approach along with an equation for the pressure field, namely the pressure-correction equation. This equation is derived by combining the momentum and continuity equations. Since pressure-based algorithms in their typical formulation result in an elliptic behavior, they need some modifications for managing the nature of the wave propagation in compressible flows. By contrast, density-based methods which are very effective for calculation of compressible hyperbolic flows become inefficient as the Mach number decreases. Although there are some tricks for convergence such as artificial compressibility or preconditioning,[46-51] practically, these methods are not well matched for calculation of flows with extensive regions of low Mach numbers, that is, Mach numbers less than 0.3. It has been shown that, even using the most sophisticated procedures, density-based algorithms are less efficient than pressure-based algorithms for incompressible flows.[52]

Most of the studies done based on the pressure-based algorithm for simulation of flows at all Mach numbers have focused on the corrections of the algorithm and simple numerical schemes such as the central difference scheme, the upwind difference scheme, or the combination of these two schemes have been used.[1-8] Issa and Javareshkian[14,15] were among the first researchers to implement a high-resolution TVD scheme into a pressure-based algorithm. Most researchers believe that the pressure-based algorithm in which all equations are solved at the same time, that is, fully coupled algorithm,[19-22] is more efficient for compressible flow simulations. Because of the nature of the coupled governing equations, these methods are less efficient, in terms of numerical cost. Most of the studies have been performed on steady flows. In most cases, transient flows have not been studied at all, because the formulations have been derived in steady form.

It can be said that, so far, no research has been carried out on the implementation of WENO family schemes for the development of pressure-based algorithms to study shocks and discontinuities in compressible flows. The main objective includes the development of a method for simulation of flows at all Mach numbers by extending the formulation to ensure all properties, especially shock-capturing. This method is developed in a unified formulation that can be used for one- and two-dimensional, compressible and incompressible flows. Also, it is suitable for both steady and unsteady flows. Although the study of viscous flows is not within the scope of the present work, the method is developed in a way that is appropriate for studying viscous and inviscid flows. In the present work, for the first time, the discretization details and linearization procedure of the equations by using the WENO scheme in the pressure-based framework are introduced. The paper ends with the simulation of flows in different regimes for the assessment of general features of the developed method in shock and discontinuity capturing. The results are compared either with available theoretical solutions or with other numerical solutions reported in literatures. For this purpose, a density-based code is used which has been written based on the method presented in Reference 53 and, its results are computed and presented. It is shown that the developed method has the same accuracy as the density-based algorithm in unsteady compressible flows, while the developed method has a lower computational cost. Also, the results reported in the literatures related to the TVD pressure-based method are used for comparison in steady flows and shock tube test case.

2 | GOVERNING EQUATIONS AND ALGORITHM

Regardless of the body forces, the mathematical models expressing transport of mass, momentum, and scalar flux can be summarized as follows:

$$\frac{\partial \rho}{\partial t} + \frac{\partial \left(\rho U_j\right)}{\partial X_j} = 0 \tag{1}$$

$$\frac{\partial \left(\rho U_j\right)}{\partial t} + \frac{\partial \left(\rho U_j U_i - \tau_{ij}\right)}{\partial X_j} = 0 \tag{2}$$

$$\frac{\partial \left(\rho \phi\right)}{\partial t} + \frac{\partial \left(\rho U_j \phi - \mathscr{q}_j\right)}{\partial X_j} = S^{\phi} \tag{3}$$

The stress tensor and scalar flux vector are usually expressed in terms of basic independent variables. The scalar flux vector for energy equation is usually given by Fourier's law:

$$\mathscr{q}_j = \Gamma \frac{\partial T}{\partial X_j} \tag{4}$$

The stress tensor for a Newtonian fluid is

$$\tau_{ij} = -P\delta_{ij} \overbrace{- \frac{2}{3}\mu \frac{\partial U_k}{\partial X_k}\delta_{ij} + \mu\left(\frac{\partial U_i}{\partial X_j} + \frac{\partial U_j}{\partial X_i}\right)}^{\text{viscous terms}} \tag{5}$$

In the present work, although the inviscid flow (viscous terms $\cong 0$) is considered, but the method is developed in a way that is appropriate for studying viscous and inviscid flows. Equations of continuity, momentum, and energy equations can each be rewritten into the following general transport equation that is helpful for the presentation of the general discretization Equation (6):

$$\frac{\partial \left(\rho \phi\right)}{\partial t} + \frac{\partial \left(\rho U_j \phi\right)}{\partial X_j} = S^{\phi} \tag{6}$$

where ϕ can equal 1, U_1 or U_2 and e for continuity, momentum and energy equations, respectively. The nonlinear parts of the momentum and the energy equations are explicitly considered in the source term, S^{ϕ}. For inviscid flows, S^{ϕ} equals 0 for the continuity equation, $-\frac{\partial P}{\partial x}$ and $-\frac{\partial P}{\partial y}$ for the momentum equation in x and y direction and, $-P\left(\frac{\partial U_1}{\partial x} + \frac{\partial U_1}{\partial y}\right) + \frac{\partial}{\partial x}\left(\Gamma \frac{\partial T}{\partial x}\right) + \frac{\partial}{\partial y}\left(\Gamma \frac{\partial T}{\partial y}\right)$ for the energy equation. To complete the governing equations, an equation of state is needed. In this paper, the perfect gas equation is considered as the equation of state as follows:

$$P = \rho R T \tag{7}$$

In the current study, the discrete form of general equation is obtained by employing the finite volume method based on a general coordinate structured grid shown in Figure 1.

For the sake of brevity, the derivation of the two-dimensional discretized equations is considered with reference to only one cell face of the control volume, namely *e*. the derivation for other cell faces can be performed similarly. The following equation is obtained by using the divergence theorem for general transport equation, Equation (6), over each control volume:

$$\frac{\delta V}{\delta t}\left((\rho\phi)_{CC}{}^{m+1} - (\rho\phi)_{CC}{}^{m}\right) + I_e - I_w + I_n - I_s = S^{\phi}\delta V \tag{8}$$

The flux, I, includes the convective flux, I^C, and the diffusive flux, I^D. The interpolation of the diffusion term does not have any visible effect, while the method of calculating the average conveted (cell face) value of the dependent flux

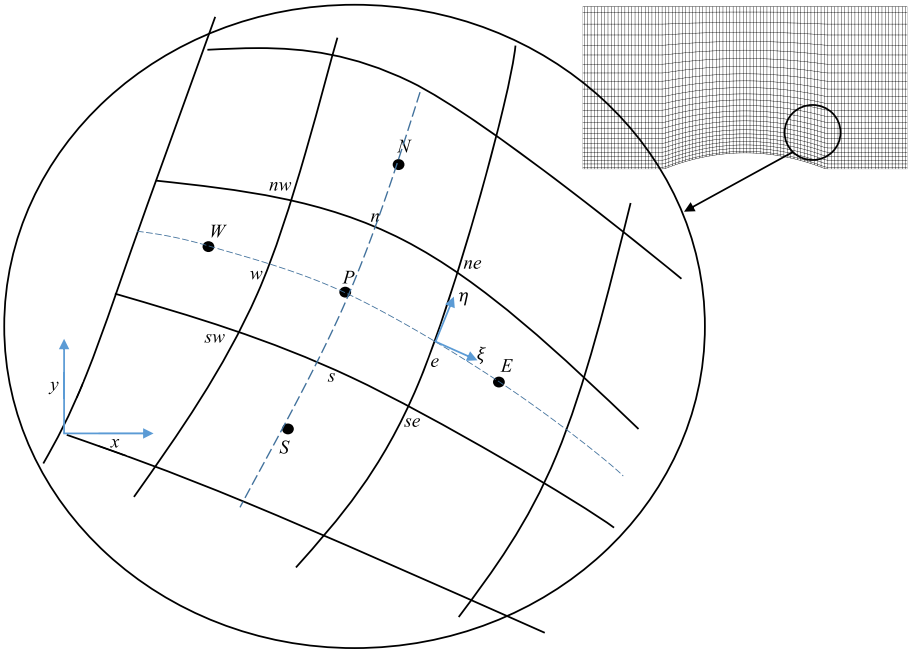

FIGURE 1 Control volume arrangement and nomenclature [Colour figure can be viewed at wileyonlinelibrary.com]

(e.g., ϕ_e) plays an important role and, it affects the accuracy, numerical oscillation, conservation and boundedness of the numerical scheme. In the present work, the diffusion term is approximated by a central difference scheme. As an example, it can be written for cell-face e as follows:

$$I_e^D = \mathcal{D}_e\left(\phi_{CC} - \phi_E\right) \tag{9}$$

To calculate the convective flux, a method must be used that is able to capture sharp discontinuities like shock waves and contact discontinuities. The convective flux is calculated as:

$$I^C = I^{C^{\text{upwind}}} - \left(I^{C^{\text{upwind}}} - I^{C^{\text{WENO}}}\right) \tag{10}$$

Equation (11) is obtained by substituting Equation (10) into Equation (8).

$$\begin{aligned}
&\frac{\delta V \rho_{CC}^m}{\delta t}\left({\phi_{CC}}^{m+1} - {\phi_{CC}}^m\right) + \left(I_e^{C^{\text{upwind}}} + \mathcal{D}_e\left(\phi_{CC}^{m+1} - \phi_E^{m+1}\right) - F_e\phi_{CC}^{m+1}\right) - \left(I_w^{C^{\text{upwind}}} + \mathcal{D}_w\left(\phi_W^{m+1} - \phi_{CC}^{m+1}\right) - F_w\phi_{CC}^{m+1}\right)\\
&\quad + \left(I_n^{C^{\text{upwind}}} + \mathcal{D}_n\left(\phi_{CC}^{m+1} - \phi_N^{m+1}\right) - F_n\phi_{CC}^{m+1}\right) - \left(I_s^{C^{\text{upwind}}} + \mathcal{D}_s\left(\phi_S^{m+1} - \phi_{CC}^{m+1}\right) - F_s\phi_{CC}^{m+1}\right)\\
&= S^\phi \delta V + \left[\left(I_e^{C^{\text{upwind}}} - I_e^{C^{\text{WENO}}}\right) - \left(I_w^{C^{\text{upwind}}} - I_w^{C^{\text{WENO}}}\right) + \left(I_n^{C^{\text{upwind}}} - I_n^{C^{\text{WENO}}}\right) - \left(I_s^{C^{\text{upwind}}} - I_s^{C^{\text{WENO}}}\right)\right]^m
\end{aligned} \tag{11}$$

The difference between the high-order and low-order convection fluxes is shifted to the right of the equation. Substituting the upwind convection terms, it is obtained as:

$$\begin{aligned}
&\left(\frac{\rho\delta V}{\delta t} - F_e + \mathcal{D}_e + F_w + \mathcal{D}_w - F_n + \mathcal{D}_n + F_s + \mathcal{D}_s\right)^m {\phi_{CC}}^{m+1}\\
&\quad = H\left(\phi^{m+1}\right) + \left(S^\phi \delta V\right)^m + \left(\frac{\rho\delta V}{\delta t}\phi_{CC}\right)^m\\
&\quad\quad + \underbrace{\left[\left(I_e^{C^{\text{upwind}}} + I_e^{C^{\text{WENO}}}\right) - \left(I_w^{C^{\text{upwind}}} + I_w^{C^{\text{WENO}}}\right) + \left(I_n^{C^{\text{upwind}}} + I_n^{C^{\text{WENO}}}\right) - \left(I_s^{C^{\text{upwind}}} + I_s^{C^{\text{WENO}}}\right)\right]^m}_{\text{differed correction terms}}
\end{aligned} \tag{12}$$

In order to guarantee the stability of the solution, only the upwind convective fluxes included in $H(\phi^{m+1})$, are considered implicitly. For improving the accuracy of the results, the contribution of the other flux parts like deferred correction

terms, $S^{\phi}\delta V$ and $((\rho\delta V/\delta t)\phi_{CC})$,are evaluated based on known quantities in the old time-step (mth), that is, explicitly. These terms are added to the source term, S^{ϕ}, and form a new source term as:

$$S\prime^{\phi} = S^{\phi} + \text{Terms calculated explicitly} \tag{13}$$

The new source term, S'^{ϕ}, contains quantities arising from non-orthogonality, external sources, dissipation terms, deferred correction terms, and $(\rho\delta V/\delta t)\phi_{CC}$ of the old time-step/iteration level. With the preceding above consideration, the general discretized equation takes the form

$$a_{CC}{\phi_{CC}}^{m+1} = \sum_{k}^{E,W,N,S} a_k \phi_k^{\mathrm{m}+1} + S'^{\phi} \tag{14}$$

where $H\left(\phi^{m+1}\right) = \sum_{k}^{E,W,N,S} a_k \phi_k^{\mathrm{m}+1}$ and the a_k are coefficients whose expressions can be driven using upwind difference scheme for convective terms and include diffusion terms. a_{CC} is as follows:

$$a_{CC} = \frac{\rho\delta V}{\delta t} + a_E + a_W + a_N + a_S \tag{15}$$

Computations of high-order convective fluxes including mass, momentum and energy fluxes are performed by approximate Riemann solver which uses the WENO scheme for interpolation from the nodes at the neighboring points. The high-order convective flux can be written as

$$I_e^{C^{\mathrm{WENO}}} = \frac{1}{2}\left(I^{C^{\mathrm{Left}}} + I^{C^{\mathrm{Right}}} - \underbrace{\widetilde{R}|\widetilde{\Lambda}|\widetilde{L}\left(Q_e^{\mathrm{Right}} - Q_e^{\mathrm{Left}}\right)}_{\text{dissipation term}} \right) \tag{16}$$

Tilde, $\sim$, indicates that the values in matrix are considered based on Roe average. To calculate the eigenvalues (Λ), left (L), and right (R) eigenvectors, the appropriate matrixes for curvilinear coordinate system which have been presented in Reference 54 are used. For a curvilinear grid, conservative variable vector and convective flux vector are shown by Q and I^{ξ}, in e cell face, as follows:

$$Q = \begin{pmatrix} \rho \\ \rho U_1 \\ \rho U_2 \\ \rho e \end{pmatrix}, I_{\xi} = \begin{pmatrix} \rho U_{\xi} \\ \rho U_{\xi} U_1 + P G_{\xi_1} \\ \rho U_{\xi} U_2 + P G_{\xi_2} \\ \rho U_{\xi}\left(e + P/\rho\right) \end{pmatrix}$$

$$U_{\xi} = U_1 G_{\xi_1} + U_2 G_{\xi_2}$$

$$G_{\xi_1} = y_{ne} - y_{se}, \quad G_{\xi_2} = -(x_{ne} - x_{se}) \tag{17}$$

where U_1, U_2, P, e are the velocity in x and y direction, the static pressure and the internal energy, respectively. ξ and η are the coordinate axes in the curvilinear coordinate system. The first, the mass flux, and fourth, the energy flux, terms of the flux vector (I_{ξ}) are in line with the curvilinear coordinate system, (ξ, η). The second and third terms, the momentum fluxes, are in line with a Cartesian coordinate system.

Obviously, any multidimensional high-order scheme can be used into the procedure and this is one of the benefits of the developed method. For the sake of completeness in the present work, a five-point stencil WENO reconstruction is considered. It is known as the third-order WENO reconstruction, WENO3R, which can be written in the following form to construct left and right states at the cell boundary from the solution available at neighboring points.

$$Q_e^{\mathrm{Left}} = \frac{\omega_1}{2}\left(-Q_W + 3Q_{CC}\right) + \frac{\omega_2}{2}\left(Q_{CC} + Q_E\right) \tag{18}$$

$$Q_w^{\text{Right}} = \frac{\omega_1}{2}(Q_W + Q_{CC}) + \frac{\omega_2}{2}(3Q_{CC} - Q_E) \tag{19}$$

Each two neighboring points form a section which is called stencil. ω_1, ω_2 are the nonlinear weight factors and are defined as

$$\omega_1 = \frac{\alpha_1}{\alpha_1 + \alpha_2}, \qquad \omega_2 = \frac{\alpha_2}{\alpha_1 + \alpha_2} \begin{Bmatrix} \alpha_1 = \frac{\lambda_1}{(\beta_1 + \epsilon)^2} \\ \alpha_2 = \frac{\lambda_2}{(\beta_2 + \epsilon)^2} \end{Bmatrix} \tag{20}$$

β_1, β_2 are called smoothness indicators which are defined as

$$\beta_1 = (Q_{CC} - Q_W)^2, \qquad \beta_2 = (Q_E - Q_{CC})^2 \tag{21}$$

Equations (18)–(21) indicate that if the smoothness indicator increases, the function Q becomes smoother in the stencil. Therefore, if there is a discontinuity such as shock wave in the stencil, its weight approaches to zero, and the other stencil becomes more effective. In Equation (18), the linear weighting coefficients, λ_1, λ_2, equal 1/3 and 2/3, respectively. For Equation (19), these coefficients are different and $\lambda_1 = 1/3$, $\lambda_2 = 1/3$. It is recommended to consider $\epsilon = 10^{-6}$ for eliminating zero denominators.

2.1 | Solution algorithm

Most of contemporary pressure-based methods employ a sequential iteration technique in which the different conservation equations are solved one after another. This iteration level is usually considered as outer iteration. The common approach taken for performing continuity is to combine the continuity equation with momentum to derive an equation for pressure, namely pressure-correction. For unsteady test cases, the present work employs the PISO algorithm introduced by Issa.[55] In PISO algorithm, at each time step, the discretized equations are implicitly solved by a sequence of predictor and corrector steps which are considered as inner iteration. Issa has shown that if the number of internal iteration loops is more than one, the time accuracy will be equivalent to second order accuracy. Also, Xiao et al (fig. 8(B) of Reference 22) have shown that the choice of time integration scheme does not have any visible effect in the computed results. PISO algorithm is especially efficient for unsteady flows, as it does not involve expensive iteration. For steady test cases, SIMPLE algorithm is employed. At each time step, linear equations of momentum and scalar are solved by strongly implicit procedure and pressure-correction equation is solved by Bi-conjugate gradient method.

3 | PRESENTING THE RESULTS

In the coming section, both two-dimensional and one-dimensional inviscid flows are computed. The results are compared either with existing numerical solutions obtained by the others or with analytical solution, where available.

The first validation is the flow through a shock tube in which subsonic, transonic, and supersonic flows are computed and compared with analytical solution presented in Reference 56. Then, the results of inviscid unsteady flow through two-dimensional Riemann problem defined by Lax and Liu[57] are compared with the existing numerical simulation, including the WENO3R density-based results presented in Reference 57. For the third test case, the steady bump channel flows ranging from subsonic to supersonic regime are investigated and compared with the TVD-Van Leer results reported in literature. This section ends with a supersonic steady flow test case through a ramp with $M_{in} = 2$.

3.1 | One-dimensional shock tube

An important practical application of unsteady one-dimensional flow is the shock tube problem. Figure 2 illustrates the initial condition of the shock tube which is a long constant area tube divided in two sections by a diaphragm. One section is filled with high pressure gas and the other section is filled with the low-pressure gas. At $t > 0$, the diaphragm

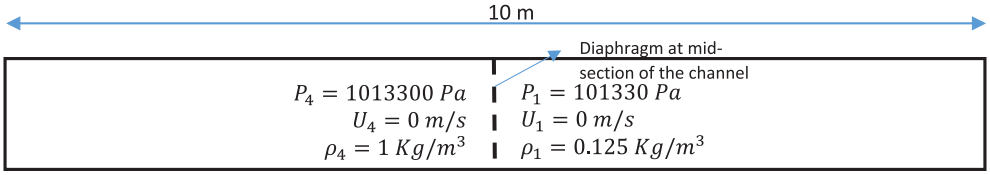

FIGURE 2 the initial condition of shock tube test case1 [Colour figure can be viewed at wileyonlinelibrary.com]

raptures and a shock wave travels to low pressure region, while an expansion wave propagates to high pressure region with the speed of sound, h_4, at its front. Theoretically, since the gas state in shock region is obtained by an irreversible process and the gas in expansion region is obtained by an isentropic process (constant entropy, $T_2 \neq T_3$), a contact discontinuity exists between regions. Therefore, four different regions have to be captured, as a result of a numerical computation.

For this test case, the pressure ratio is considered $P_4/P_1 = 10$ and, the number of grid points and time step equal 100 and 0.000005 s, respectively. The CFL (Courant-Friedrich-Lewy) number based on speed of sound (CFL No. $= (U_1 + c)\delta t/\delta x$) is considered 0.035. It has been shown that if the CFL is less than 0.1, the shock tube numerical solution is independent of the CFL.[58] Based on ideal gas assumption, the initial temperatures of $T_4 = 352.89$, $T_1 = 282.31$ K are calculated. Same gases are chosen on both sides of the diaphragm ($C_P = 1005$(J/kg K), $\gamma = 1.4$). For all flow variables, zero normal gradient boundary conditions are imposed at all boundaries. The final simulation time is considered 0.006 s and, the expansion and shock waves do not reach the outlet boundary at this time. Figure 3 shows the dimensionless pressure, dimensionless density, velocity and Mach No. variations along the shock tube at $t = 0.006$ s computed with different schemes and algorithms. The pressure and density have been normalized by reference values at high pressure region at initial condition. Guided by the findings from Figure 3, it is clearly seen that simulation results reproduce the discontinuities in the velocity, pressure, density and Mach number with very good accuracy and all these field parameters are in good agreement with the analytical (exact) solution. Predicted pressure distributions in Figure 3(A) show that the pressure-based WENO3R result is well consistent with that of the density-based WENO3R. However, the WENO3R pressure-based result is a little bit more accurate than the others in the expansion region. In Figure 3(B), comparison of the density variations along the shock tube for different schemes well depicts the performance of schemes. In case of the first order upwind scheme, the overall smearing of the contact discontinuity is mainly attributed to the first-order accuracy used for convective fluxes which produces excessive false diffusion. In zoomed views of Figure 3(B), the results of density show that the developed pressure-based WENO3R method is more accurate than the density-based results. The contact discontinuity position has been exactly predicted using this method. Based on the presented results, it is clear that all schemes in the shock discontinuity have almost enough accuracy, but the accuracy of the results in contact discontinuity is quite different for different schemes. It seems that this zone is more sensitive to numerical accuracy and this issue must be considered in numerical simulations. Figure 3(C) shows that the velocities of the shock wave and the head of expansion fan have been well predicted.

In addition to qualitatively comparing the results, l^2-norms of filed variables are also calculated in order to quantify the results quantitatively as

$$\|\varphi\|_2 = \sqrt{\sum_{k=1}^{k=\text{Number of Cells}} |\varphi_k^{\text{ref}} - \varphi_k|^2} \tag{22}$$

The analytical solution is considered as reference solution. The computed l^2-norms have been tabulated in Table 1 for different schemes and algorithm. The l^2-norms have been computed at $t = 0.006$ s for a grid with 100 cells. Although the pressure-based WENO3R method yields smaller l^2-norms, but it is clear from the results presented in Figure 3 that the results for both algorithms (WENO3R density-based/pressure-based) are consistent.

For the sake of completeness, pressure-based TVD results for density variation presented in Reference 14 are compared with pressure-based WENO3R results. In Figure 4, as it is seen, the WENO3R solution is steeper and more accurate in contact discontinuity and shock regions. It is obvious because WENO3R has second order accuracy in these regions while TVD switches to the first order accuracy in discontinuities. Of course, coarse grid should be used to better evaluate the accuracy of the WENO and TVD schemes. Actually, the main idea of using high-order accuracy in high resolution schemes is to control the computational cost by reducing the number of grid cells. Since the result of the TVD scheme has been used based on Reference 14, it is not possible to compare on a coarse grid.

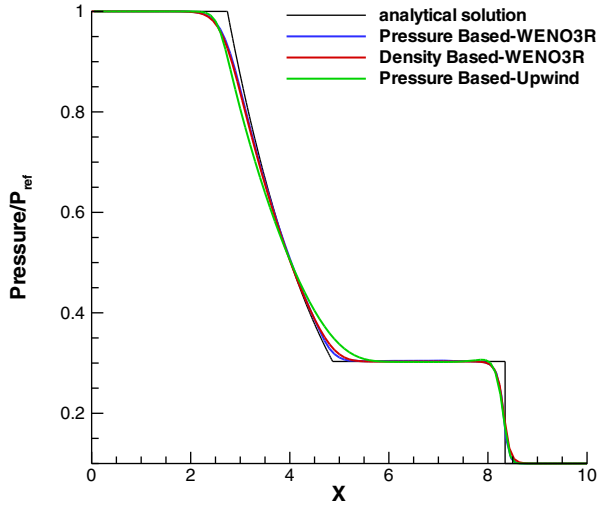

(A) Normalized pressure distribution along the shock tube

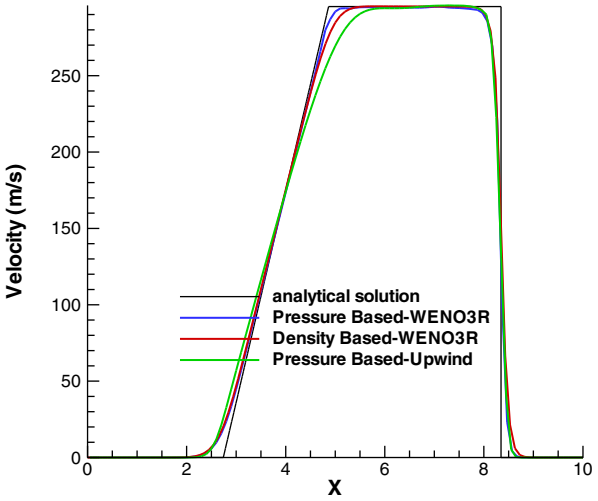

(C) velocity distribution along the shock tube

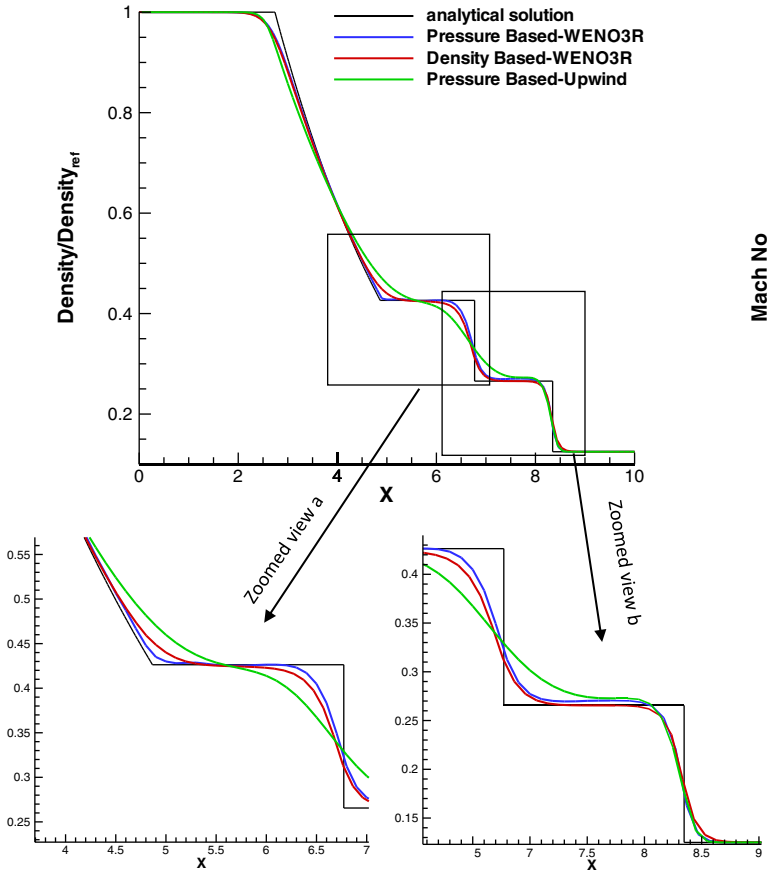

(B) Normalized density distribution along the shock tube

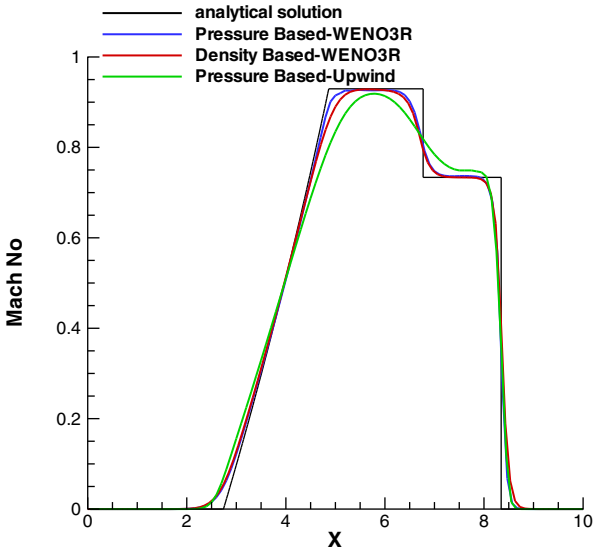

(D) Mach No. distribution along the shock tube

FIGURE 3 Comparison of the shock tube results at $t = 0.006$ s [Colour figure can be viewed at wileyonlinelibrary.com]

3.2 | Two-dimensional Lax configuration

For the next test case, unsteady two-dimensional (2-D) Lax configuration is investigated, namely configuration 16. The performance of five-point stencil high-resolution WENO3R scheme is discussed by using selected benchmark test case. This test case has been described by Lax and Liu.[57] The interested reader is referred to their archival

TABLE 1 Computed l^2-norms of field variables for shock tube, for the solutions obtained by various schemes/algorithm

Scheme/algorithm	Density	Pressure	Mach
Upwind-pressure based	8.184635E-02	7.86797E-02	1.724959E-01
WENO3R-pressure based	5.081382E-02	4.98245E-02	1.286552E-01
WENO3R-density based	5.859061E-02	5.53074E-02	1.436417E-01

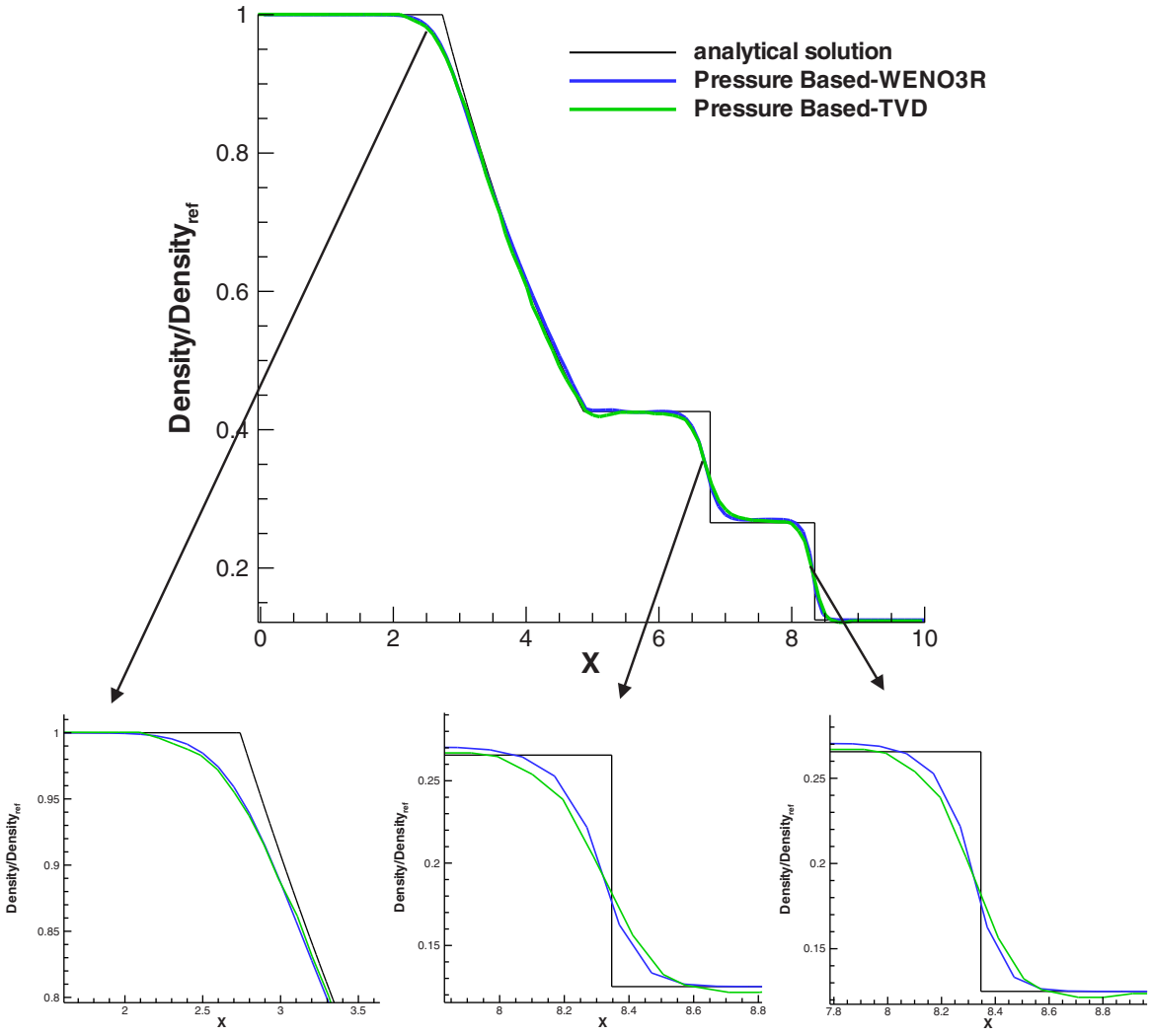

FIGURE 4 comparing the TVD[14] and WENO3R pressure-based results for density in the shock tube [Colour figure can be viewed at wileyonlinelibrary.com]

manuscript for the details of the wave structures of each configuration for other benchmark test cases. 19 configurations have been presented by Lax and Liu.[57] Actually, this configuration is a kind of 2D shock tube with different pressure ratios, that is, different shock strength in the same field. Using configuration 16 as test case, the shock-shock and expansion-shock interaction can be investigated. Also, the performance of developed WENO3R pressure-based scheme is evaluated in unsteady 2-D flow. Figure 5 indicates the initial condition of the test case. The ratio of specific heats, γ, is considered 1.4. For the sake of brevity, just the pressure and density contours are presented.

Zero normal gradients for all flow variables are imposed at the domain boundaries. One of the most common methods for boundary conditions is to consider virtual cells behind the boundaries. For a wall where the cells end there, the reflexive boundary condition is shown in Figure 6. For example, the fifth order accuracy requires 3 virtual cells that are shown in the figure.

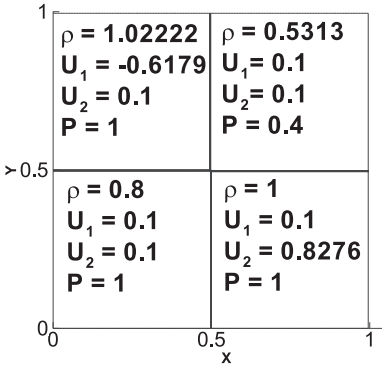

FIGURE 5 Initial conditions for two-dimensional Riemann test case (configuration 16) defined by Lax and Liu[57]

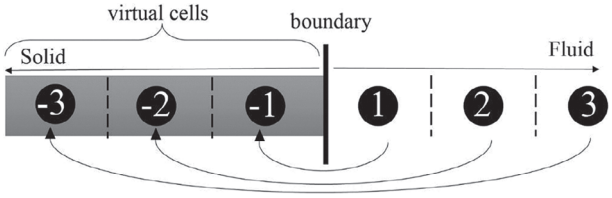

FIGURE 6 Boundary and virtual cell conditions according to the accuracy of the interpolation scheme near boundary

3.2.1 | Grid study

Lax configuration is a numerical test case rather than a physical test case. So, there is no analytical solution or experimental data to quantify the results. In these cases, normally, the computed results with a fine grid are considered as reference solution. For this aim, in this sub-section a grid study is performed and the results of this study are presented in Figures 7 and 8. Four grid sizes of 100×100, 200×200, 400×400, and 800×800 are considered. To examine the results more quantitatively, Figure 8 shows the density distributions along the diagonal of the geometry. Computed results using pressure-based WENO3R show that results do not change with increasing the grid size more than 400×400 cells. Additionally, Figure 9 illustrates that using a grid with fine mesh may drastically increase the CPU elapsed time. So, in the current study, the grid size 400×400 is chosen for performance investigation of the developed pressure-based WENO3R method (Table 2).

3.2.2 | Investigating Lax configuration 16 using different methods

The comparison of the results computed by using different methods is illustrated in Figure 10. The results involve expansion, shock, and contact discontinuity. The density filed obtained by the pressure-based WENO3R method is compared with the benchmark. This comparison is shown in the top row of Figure 10. The bottom row presents the density and pressure contours simulated by density-based and pressure-based algorithms. Since the range and number of lines have not been mentioned for the results presented by Lax, therefore 40 equidistant lines are considered for presenting the results in Figure 10. In part (C) of the figure, density lines obtained by WENO3R density-based (red lines) are compared with density lines (black lines) overlaid on density contour computed using the WENO3R pressure-based.

As expected, the sharp non-oscillatory gradients have been well obtained using the developed WENO3R pressure-based code. Also it can be seen that there is no significant and visible difference between the pressure-based WENO3R and density-based WENO3R results. Our investigations clearly show that from accuracy point of view, the dissipative character of the scheme is more crucial than the selection of the solution algorithm. The developed WENO3R pressure-based method well predicts the sharp gradients, especially for contact discontinuities compared with the benchmark. The reason is that the approximate Riemann solver is highly sensitive to how well a discontinuity is aligned with the underlying grid of the problem. For the test cases in which the grid is not aligned with the discontinuities, cross coupling between the Riemann problems in the different directions introduces numerical dissipation error. The developed code considers the effects of the cross coupling.

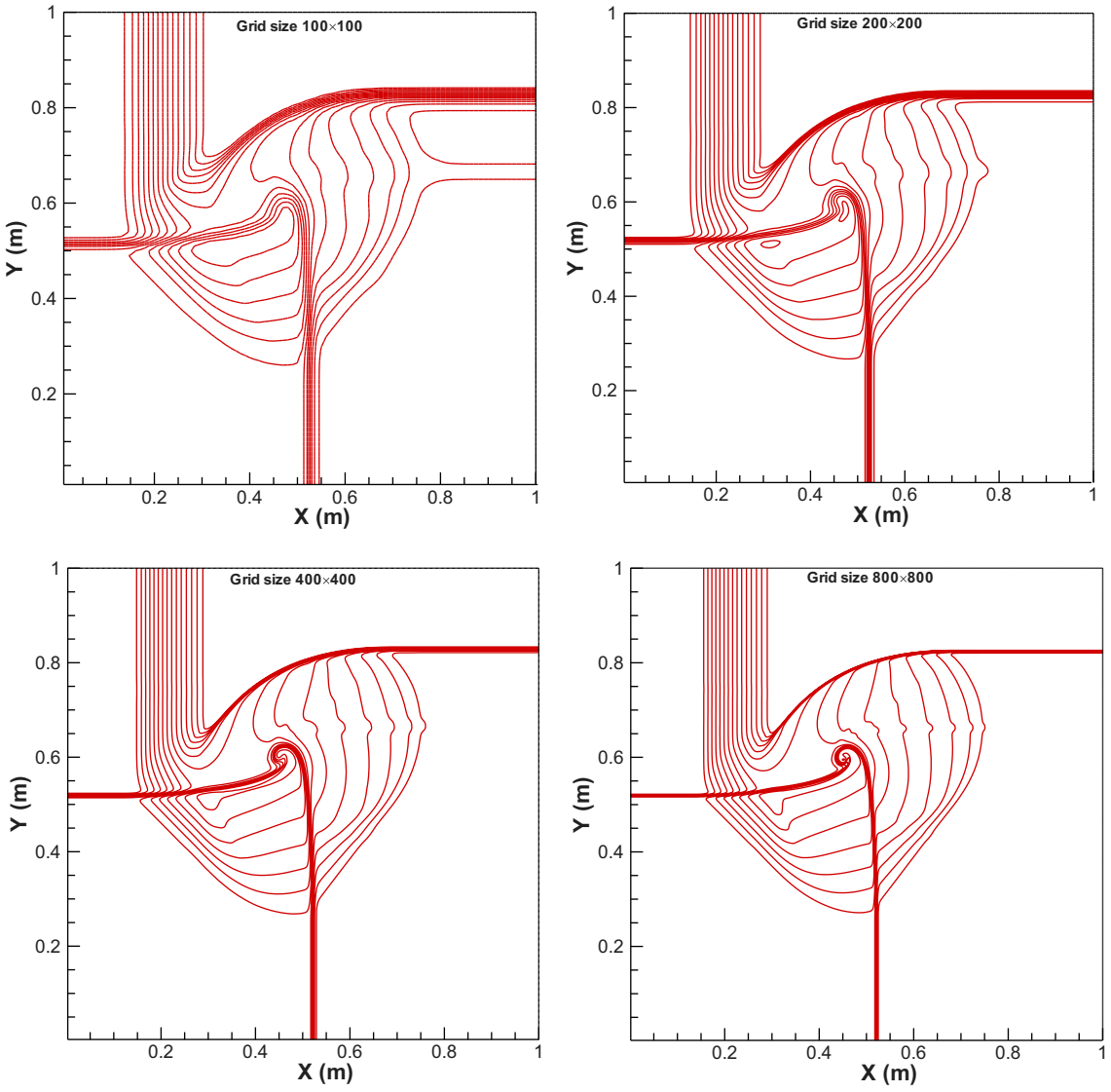

FIGURE 7 Computed results for configuration 16 at time $t = 0.2$. Comparison of density lines (0.55–1)0.15 equidistant contour lines are shown using WENO3R scheme for different grid sizes [Colour figure can be viewed at wileyonlinelibrary.com]

To quantify the results quantitatively, the l^2-norm is computed and presented in Table 3. The slight difference in computed l^2-norm means that the pressure-based algorithm, like the density-based algorithm, is suitable for simulating the flow field with discontinuities.

3.2.3 | Computational cost

All computations have been carried out using the Fortran compiler on a windows 10, 64-bit operating system made up of Core(™) i7-4790 Intel (3.6 GHz) utilizing a 16.0 GB installed memory (RAM). For configuration 16, the total CPU elapsed time obtained using pressure-based and density-based algorithms is presented in Table 4. Although we have not tried any efforts for writing optimal code, but our investigations on all Lax configurations show that from computational cost point of view, the WENO pressure-based algorithm is obviously more efficient than the WENO density-based, and the WENO pressure-based decreases the average computational cost up to 15% compared to WENO density-based. This is completely predictable. The non-linear system of governing equations and explicitly solving the equations can affect the computational costs of the density-based algorithm.

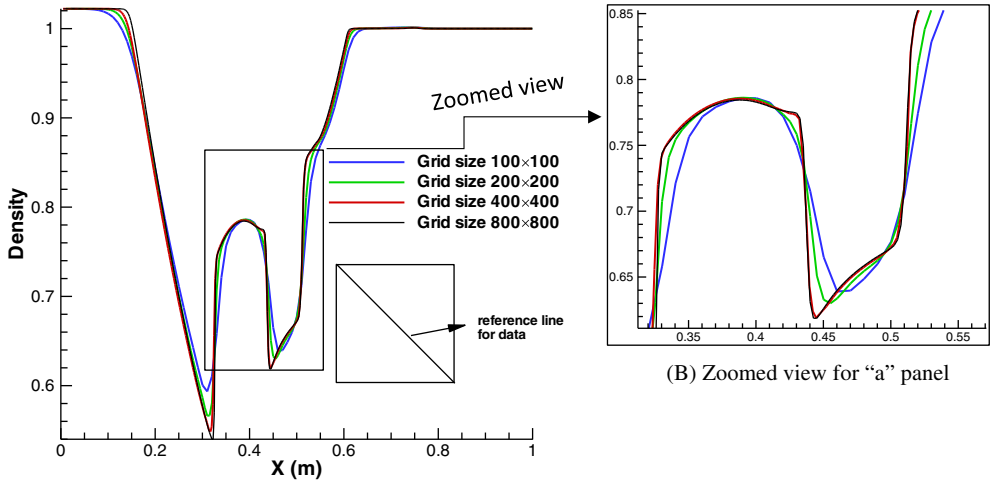

(A) Density along the reference line with negative slope

(B) Zoomed view for "a" panel

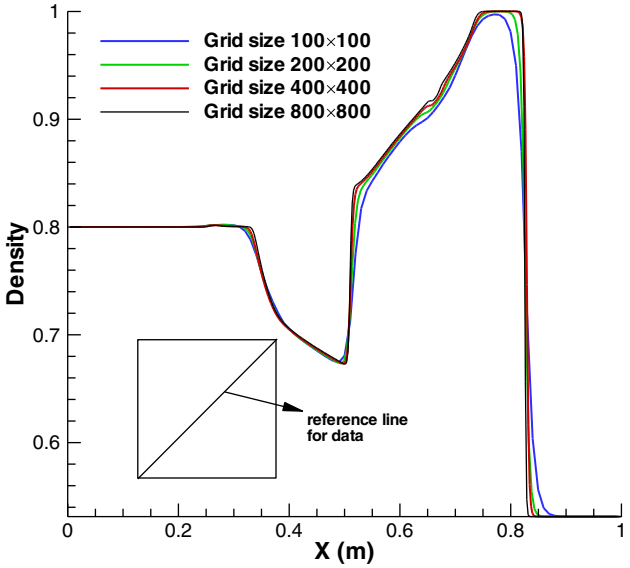

(C) Density along the reference line with positive slope

FIGURE 8 Density variation for configuration 16 along the reference lines regarding to Figure 7 [Colour figure can be viewed at wileyonlinelibrary.com]

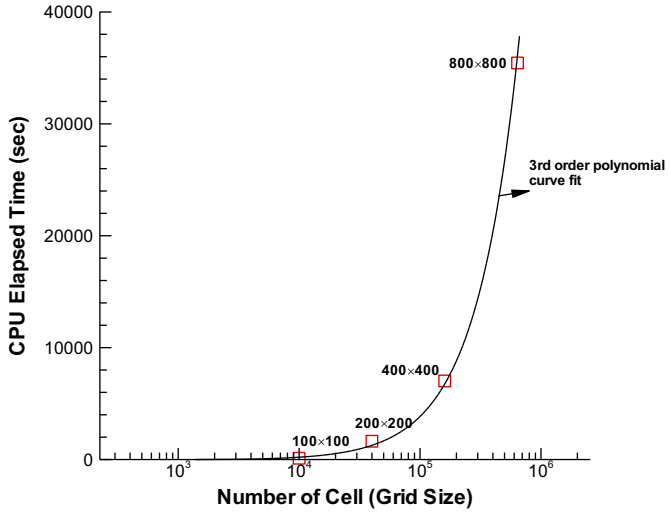

FIGURE 9 CPU elapsed time for different grid sizes, configuration 16 [Colour figure can be viewed at wileyonlinelibrary.com]

TABLE 2 CPU elapsed time for different grid sizes, configuration 16

Grid size	100 × 100	200 × 200	400 × 400	800 × 800
CPU elapsed time (s)	118.0317	1636.855	7024	35442.92

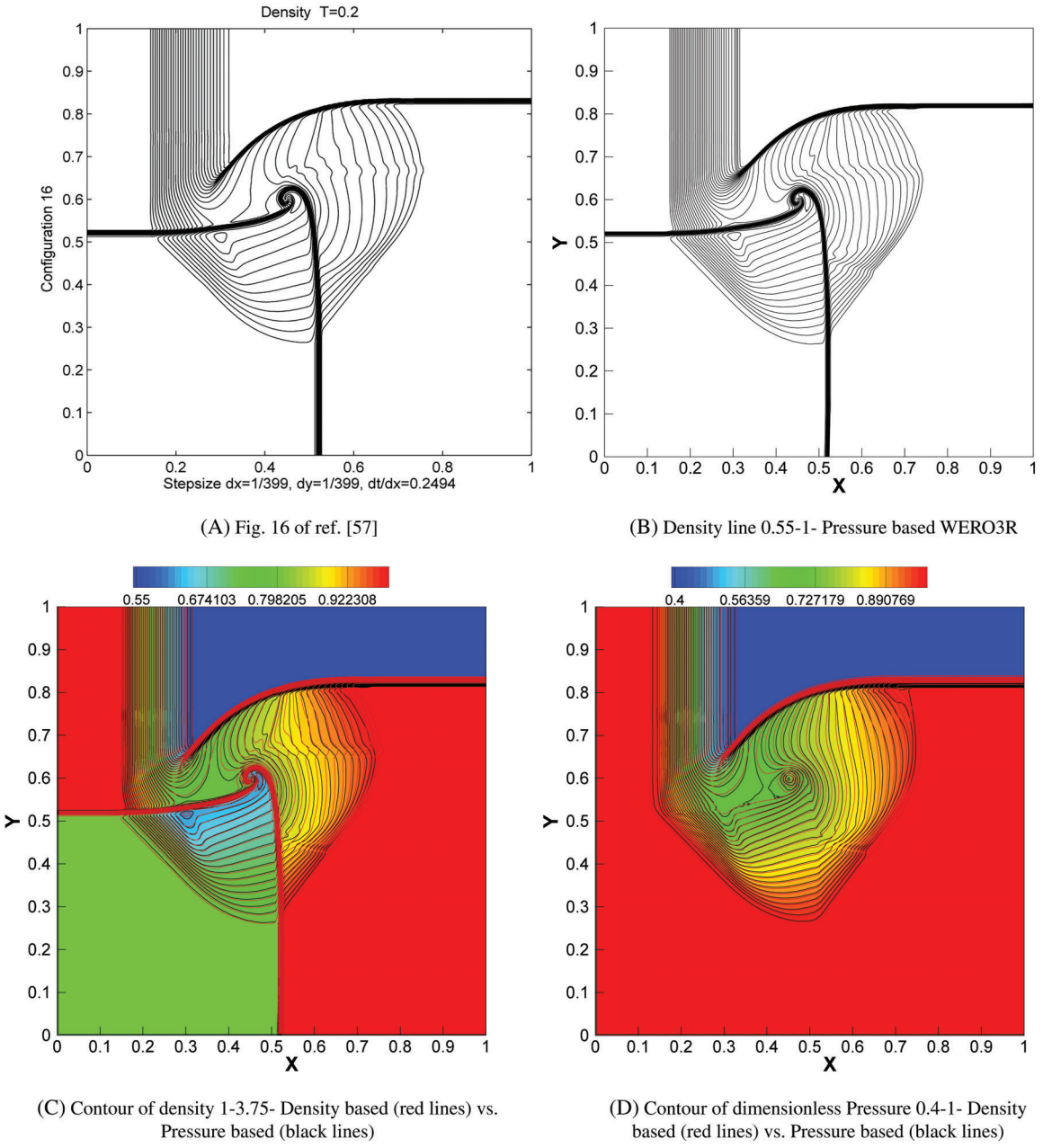

(A) Fig. 16 of ref. [57]

(B) Density line 0.55-1- Pressure based WERO3R

(C) Contour of density 1-3.75- Density based (red lines) vs. Pressure based (black lines)

(D) Contour of dimensionless Pressure 0.4-1- Density based (red lines) vs. Pressure based (black lines)

FIGURE 10 Configuration 16 at time $t = 0.2$ [Colour figure can be viewed at wileyonlinelibrary.com]

3.3 | Subsonic, transonic, and supersonic flow over a bump channel

In this section, steady flows are considered at different speeds ranging from subsonic to supersonic, over a bump inside a channel. The channel has a height of 1.0 m and a length of 2.0 m for subsonic and transonic cases, and 3 m for supersonic case. The bump has been placed at the center of the geometry on the lower wall and has a chord of 1.0 m. The channel geometry is shown in Figure 11. In this study, in cases of subsonic and transonic flows, the thickness-to-chord ratio of the bump is considered 10% and, in case of supersonic flow, it is 4%. These are test cases frequently used in literatures, for example References 15,22.

Scheme/algorithm	Density	Pressure
WENO3R-pressure based	1.2261E-01	1.2022E-01
WENO3R-density based	1.0740E-01	1.0138E-01

Note: Reference solution is obtained by a grid size 800×800.

TABLE 3 Computed l^2-norms of density and pressure fields for configuration 16 obtained by grid size 400×400

Scheme/algorithm	CPU elapsed time (s)
WENO3R-pressure based	7024
WENO3R-density based	7826

TABLE 4 CPU elapsed time for different methods, configuration 16

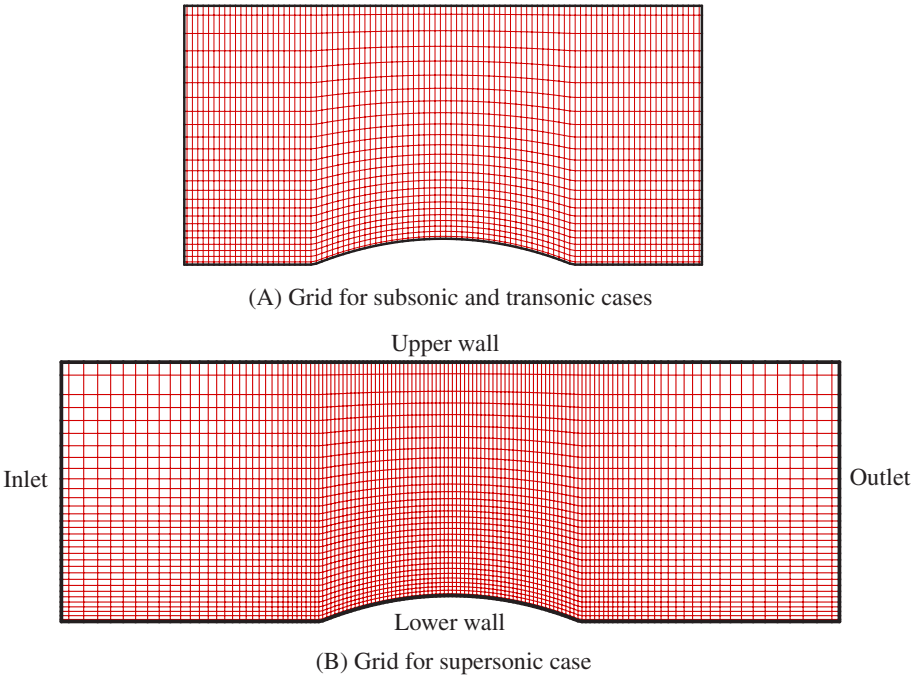

(A) Grid for subsonic and transonic cases

(B) Grid for supersonic case

FIGURE 11 Geometry and structured mesh for the flow simulation in bump channel [Colour figure can be viewed at wileyonlinelibrary.com]

3.3.1 | Subsonic test case

To simulate subsonic flow within the bumped channel, a steady inlet Mach number of $M_{in} = 0.5$ is set. Also, the pressure is specified and fixed as $P_{totall,in} = 120{,}198.9$ Pa and $P_{out} = P_{ref} = 101{,}330$ Pa, at the inlet and outlet of the channel. The reference value for temperature is specified to $T_{totall,in} = 302.55$ K. For the simulations, a structured relatively coarse grid with 98×26 cells is employed. The Mach lines overlaid on Mach contour of the simulated steady result are shown in Figure 12 using WENO3R and TVD pressure-based methods. The Mach number profile at the upper and lower walls is illustrated in Figure 13. As expected, the Mach number distribution computed using different schemes are in good agreement, because there are not any shock or discontinuity in the flow field. Almost all the schemes developed for the Euler equations are acceptable for smooth flows without strong gradients.

In case of steady simulations, the outer iteration is ended according to a fractional change criterion typically of the form.

$$\text{Residual}\,(m) = Max\left(\left|\frac{\varphi^m - \varphi^{m-1}}{\varphi_{ref}}\right|\right) < \varepsilon \tag{23}$$

where φ_{ref} are reference values at the inlet of the flow field and, ε is a small positive number. m is the iteration counter. In the present work, ε has been considered 10^{-5}. Since the accuracy of the results in the subsonic flow is almost the same for different schemes, it is better to check and compare the convergence rate in this case. Figure 14 illustrates

FIGURE 12 The Mach lines overlaid on Mach contour for bump channel, $M_{in} = 0.5$, subsonic test case

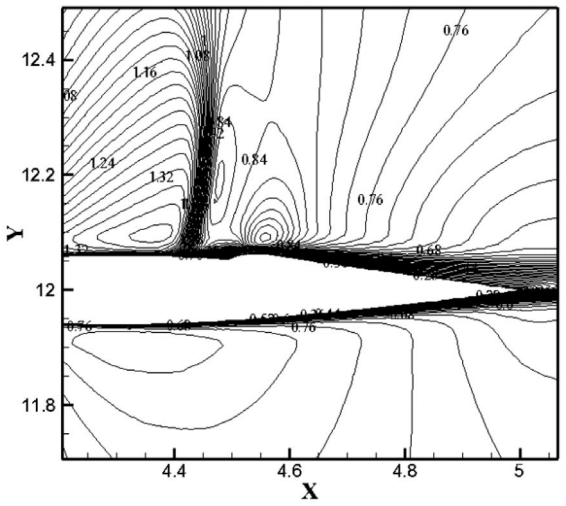

(A) Mach contour with flexibility %15

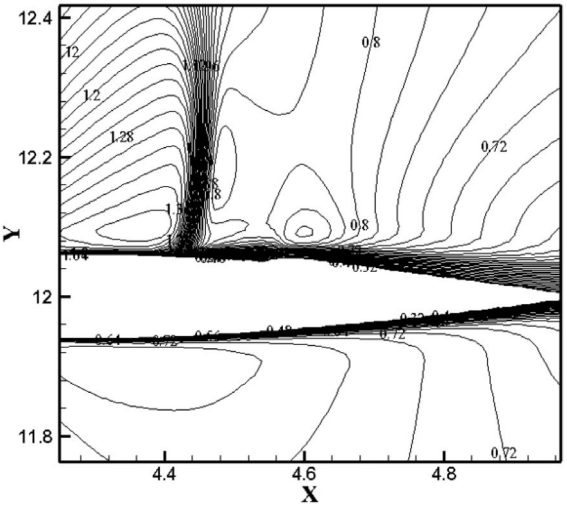

(B) Mach contour with flexibility %10

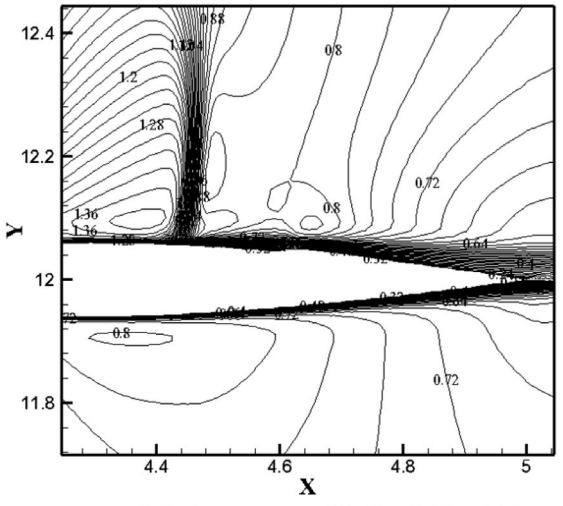

(C) Mach contour with flexibility %5

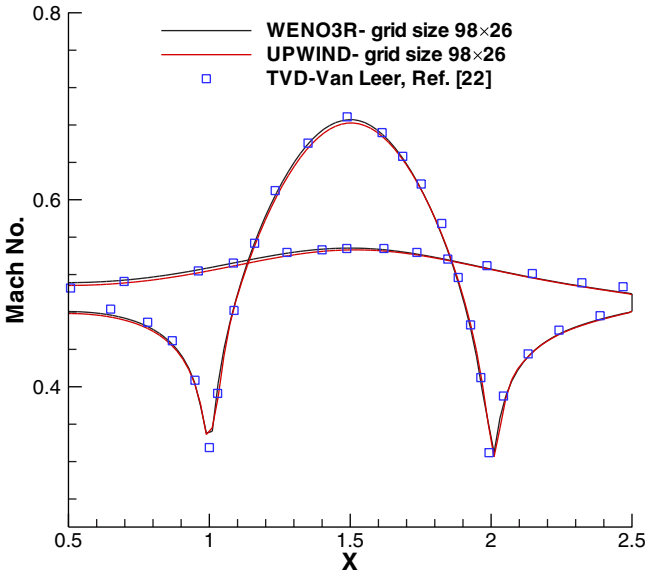

FIGURE 13 Mach number distribution along the lower and upper walls of bump channel, $M_{in} = 0.5$; computed results using Upwind and WENO3R schemes vs results from Reference 22 [Colour figure can be viewed at wileyonlinelibrary.com]

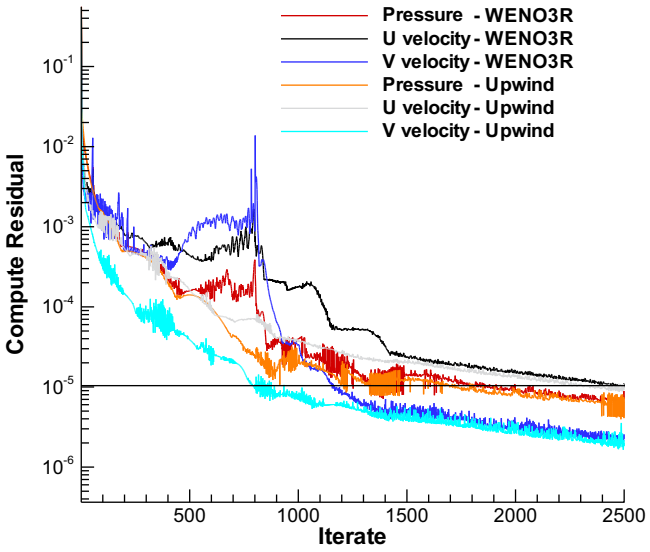

FIGURE 14 Convergence rate of the Upwind and WENO3R schemes in the sense of the local truncation error for bump channel, subsonic test case [Colour figure can be viewed at wileyonlinelibrary.com]

the convergence rate for subsonic flow in bumped channel. As it is seen, at the beginning of the convergence process, due to the reduction of dissipation in the WENO3R scheme, the WENO3R convergence process moves away from the Upwind. However, due to the increasing accuracy of the calculations, the convergence process of the WENO3R scheme improves so that in the middle of the convergence process, similar behavior is seen between the schemes. Because the deferred correction method has been employed to develop numerical method, so the convergence rate of the developed WENO3R pressure-based method is similar to first order upwind scheme, especially at the end of simulation. Actually, the convergence characteristic of the upwind scheme has been used to develop the WENO pressure-based numerical method.

3.3.2 | Transonic test case

In order to study transonic flow for the bump channel, the boundary conditions are specified in the same manner as for the previous subsonic flow case, but in the current test case, the flow speed is increased which results in a steady inlet Mach number of $M_{in} = 0.675$. The boundary conditions at inlet and outlet are specified as $M = M_{in}$, $P_{totall,in} = 137{,}498.77$, $T_{totall,in} = 314.04$ K and $P_{out} = P_{ref} = 101{,}330$ Pa,. Simulations are computed by using the same grid as used for the subsonic case. Figure 15 presents the Mach lines overlaid on Mach contour using WENO3R and TVD pressure-based methods. The Mach number distribution along the upper and lower walls is shown in Figure 16. As it is seen, for the transonic

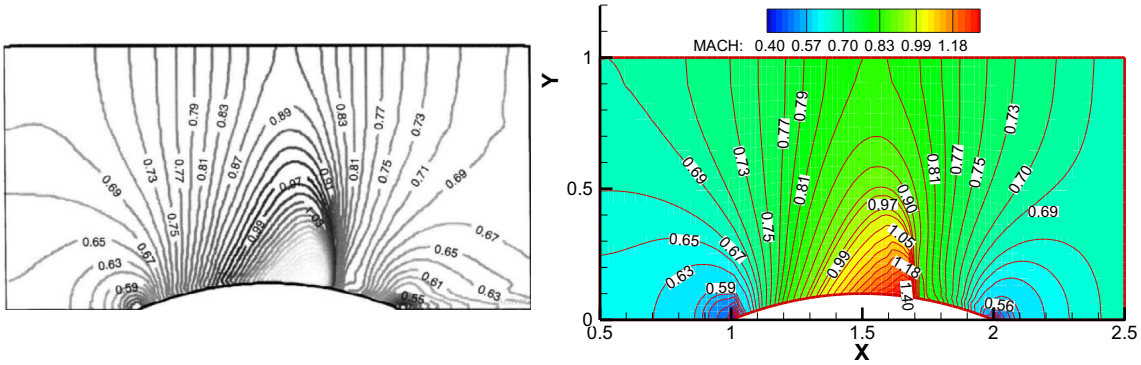

(A) TVD scheme, ref. [15] (B) WENO3R scheme

FIGURE 15 The Mach lines overlaid on Mach contour for bump channel, $M_{in} = 0.675$, transonic test case [Colour figure can be viewed at wileyonlinelibrary.com]

FIGURE 16 Mach number distribution along the lower and upper walls of bump channel, $M_{in} = 0.675$; computed results using WENO3R schemes vs results from Reference 22 [Colour figure can be viewed at wileyonlinelibrary.com]

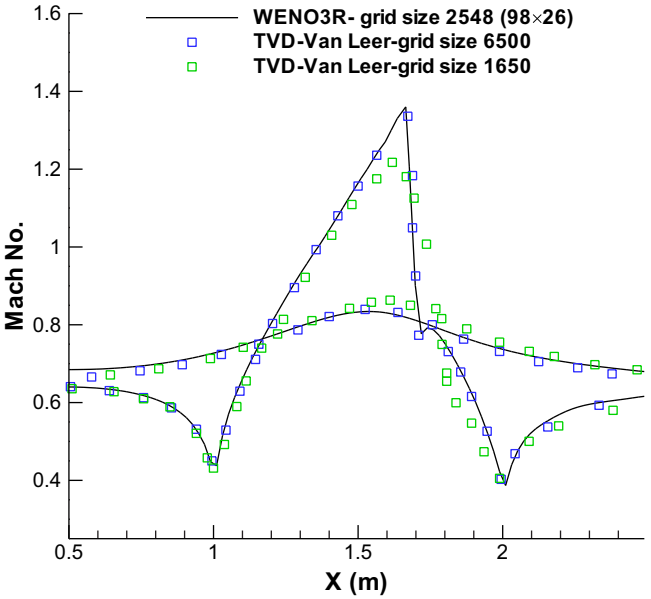

case, the computed result with WENO3R shows that a normal shock occurs on the top of bump due to increase in flow speed, because of bump curvature. Obviously, the WENO3R result is in excellent agreement with the result reported in Reference 22. The position of the shock and the amplitude of the shock are well predicted by employing the developed pressure-based method. The WENO3R result has been obtained by a coarser grid (2548 cells) compared with the TVD-Van Leer result reported in Reference 22 (6500 cells).

3.3.3 | Supersonic test case

To achieve a supersonic flow case; velocity, pressure, and temperature are specified so that inlet Mach number is set 1.4. Similar to previous test cases, the boundary conditions at inlet are specified as $M_{in} = 1.4$, $P_{in} = P_{ref} = 101{,}330\,\text{Pa}$ and $T = T_{ref} = 288\,\text{K}$. In supersonic test case, all the flow parameters are extrapolated at the outlet. In this case, the thickness-to-chord ratio equals 4%. Simulations are carried out on similar grid shown in Figure 11, with size 90×30. The Mach lines of the computed steady result are plotted in Figure 17. The Mach number profiles at channel walls are drawn in Figure 18. According to this figure, the shock is well captured using pressure-based WENO3R method. Comparing the WENO3R with TVD-Van Leer results, it can be concluded that the developed pressure-based WENO3R code predicts more accurate results even with fewer number of cells. Also, the WENO3R predicts locally subsonic region at the upper wall, while it has not been captured using TVD-Van Leer scheme. Although, Cheng et al have shown that this locally

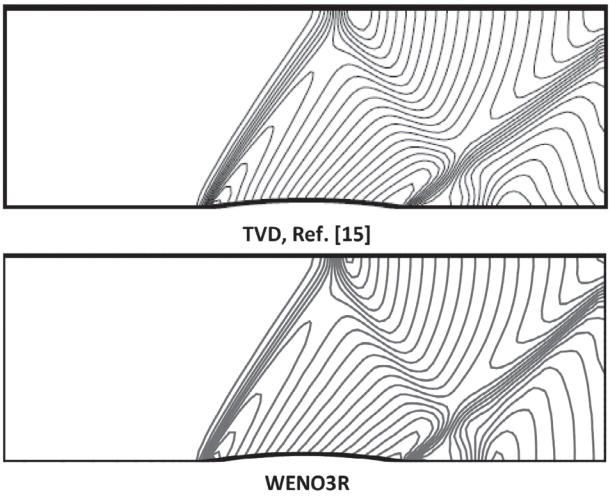

FIGURE 17 Mach lines for bump channel in supersonic, $M_{in} = 1.4$ flow; comparing WENO3R with TVD Scheme[15] using pressure-based algorithm

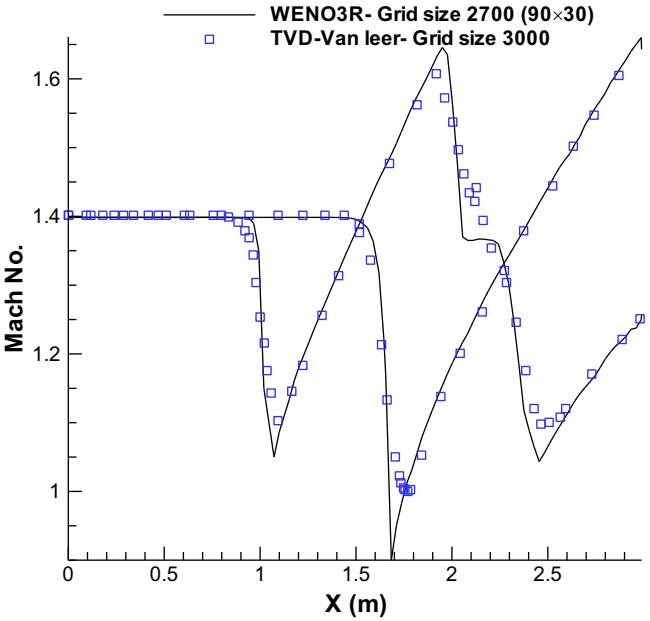

FIGURE 18 Mach number distribution along the lower and upper walls of bump channel, $M_{in} = 1.4$; computed results using WENO3R (present paper) and TVD-Van leer result from Reference 22 [Colour figure can be viewed at wileyonlinelibrary.com]

subsonic region can be captured by using a fine grid with size 14,500 cells, employing TVD-Van Leer scheme. Of course, with the explanations mentioned in the introduction, it was predictable that WENO3R would have better performance than TVD-Van Leer, however this performance is well seen at higher Mach number.

3.4 | Supersonic flow over a wedge

The final test case is steady supersonic flow over a 10° wedge. The computation is performed on a structured grid with size 90×30 shown in Figure 19. For this test case; velocity, pressure and temperature are specified so that inlet Mach number is set $M_{in} = 2$. The boundary conditions are similar to previous supersonic test case and, they are specified as $M_{in} = 2$, $P_{in} = P_{ref} = 101{,}330$ Pa and $T = T_{ref} = 288$ K. The Mach lines for WENO3R and TVD schemes are plotted in Figure 19. As it can be seen, the oblique shock captured by WENO scheme is more compact and thinner than TVD. Figure 20 indicates the Mach distribution along the upper wall and wedge surface. This figure shows that the pressure-based WENO3R method well predicts Mach after the oblique shock and the Mach Angle (β) with an error of less than one.

As can be seen from the drawn Mach lines; in some areas, especially after the shock, oscillations in the form of fine waves are seen in the lines. These slight fluctuations are sign of dispersion in the method. But the results show that this dispersion is almost completely controlled and improves the accuracy of the results. Comparing the Mach lines of the

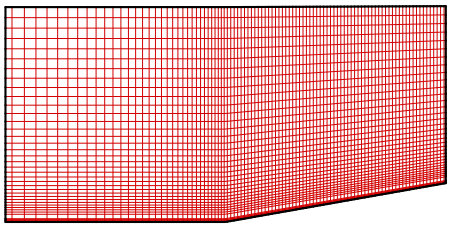

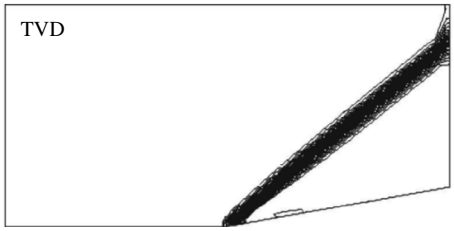

(A) TVD scheme[15]

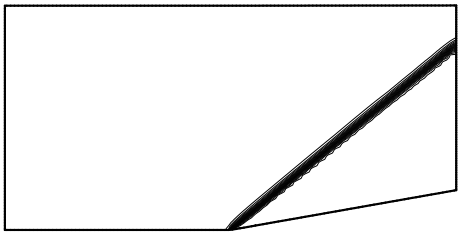

(B) WENO3R scheme

FIGURE 19 Mach lines for a 10° wedge in supersonic flow for different schemes using pressure-based algorithm [Colour figure can be viewed at wileyonlinelibrary.com]

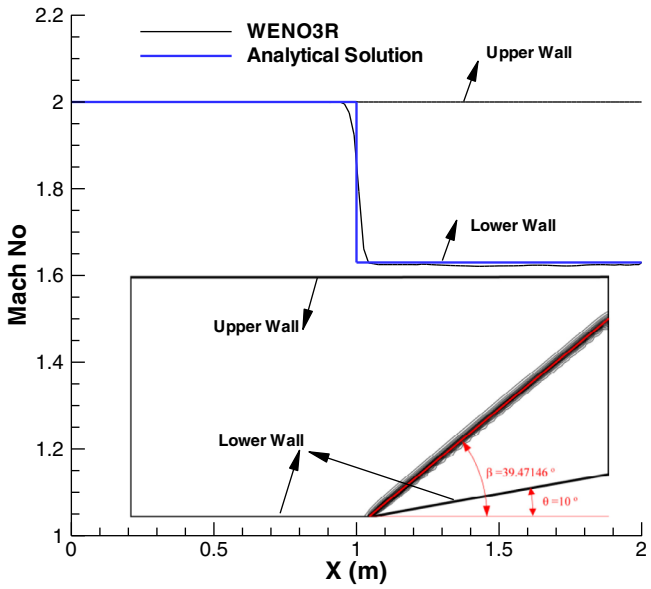

FIGURE 20 Mach distribution along upper wall and wedge surface for a 10° wedge in supersonic flow, grid size 90 × 30 [Colour figure can be viewed at wileyonlinelibrary.com]

WENO3R and TVD schemes, it can be said that although the dispersion of the WENO3R is higher than TVD scheme, however it is better controlled and, this shows the power of the WENO scheme.

4 | CONCLUSIONS AND REMARKS

A pressure-based semi-implicit procedure has been developed that incorporates bounded high-resolution WENO3R scheme and, therefore, it is well suitable for all flows including steady and unsteady. For the present study, the boundedness criterion has been determined based on WENO scheme which has been applied to the convective fluxes and

mass flux. However, this is the advantage of the present method that it has been developed in a flexible manner which any high-order scheme can be simply incorporated in to the procedure. The unsteady test cases have been simulated using WENO3R density-based algorithm and their results have been compared with WENO3R pressure-based results. The steady numerical simulations for the bumped channel have been compared with the TVD coupled pressure-based method. The comparisons showed that there is excellent agreement between the present calculations and either the analytical or other numerical solutions for one- and two-dimensional test cases in compressible flows. Also the developed WENO3R pressure-based method has a lower computational cost. It has been shown that from computational cost point of view, the developed pressure-based WENO3R is more efficient, up to 15%, than a density-based WENO3R. It has been illustrated that the WENO scheme predicts sharp non-oscillatory gradient around discontinuities and predicts discontinuities better than TVD scheme, even using lower number of grid cells. It is concluded that the developed method is suitable for simulation of compressible flows where shock waves, expansion fans and discontinuities exist.

ACKNOWLEDGEMENTS

First of all, from the bottom of my heart, I would like to express thank you for my family for their energy and understanding throughout the research, especially to my wife. We also would like to say special thank you to Mr. Alireza Moghadasi for providing us helpful supports on density-based algorithm, without your help this research would have not been the same. Mrs. Mahbube Noura helped us to improve the English language and we would like to tell thank you her for her friendly supports.

NOMENCLATURE

A	cell area (m^2)
a	coefficients in the discrete equations
C_P	specific heat capacity (kJ/kg K)
F	mass flux (kg/s)
c	speed of sound (m/s)
I	flux
P	static pressure (Pa)
Q	conservative parameter
R	right eigenvector
L	left eigenvector
Λ	eigenvalues matrix
S^{ϕ}	source term for ϕ
t	time (s)
T	temperature (K)
U	velocity vector (m/s)
U_1	x velocity (m/s)
U_2	y velocity (m/s)
$\mathcal{D}$	diffusion coefficient
X_j	$X_1 = x, X_2 = y$
ρ	density (kg/m^3)
ω	weight coefficient in WENO scheme
β	smoothness indicator
λ	weighted linear coefficient in WENO scheme
γ	specific heat ratio, C_p/C_v
Γ	thermal conductivity
μ	fluid viscosity
δt	time step (s)
δV	cell volume (m^3)
δ_{ij}	Kronecker delta, $\begin{cases} 0 & \text{if } i \neq j \\ 1 & \text{if } i = j \end{cases}$
e	Internal energy (J)

SUB INDEX

CC cell center
e Eastern cell face
w Western cell face
n Northern cell face
s Sothern cell face
ne Northern and Eastern cell faces interface
se Sothern and Eastern cell faces interface
E Eastern cell center
N Northern cell center
S Sothern cell center
W Western cell center
η the vertical coordinate axis in the curvilinear coordinate system
ξ the horizontal coordinate axis in the curvilinear coordinate system

SUP INDEX

m *m*th time step
C convection
D diffusion
Left left side of cell face
Right right side of cell face

DATA AVAILABILITY STATEMENT

The data that support the findings of this study are available from the corresponding author upon reasonable request.

REFERENCES

1. Rhie CM. Pressure-based Navier-stokes solver using the multigrid method. *AIAA J*. 1989;27(8):1017–1018.
2. Chen K-H, Pletchert RH. Primitive variable, strongly implicit calculation procedure for viscous flows at all speeds. *AIAA J*. 1991;29(8):1241–1249.
3. Shyy W, Ghent M-H, Sun C-S. Pressure-based multigrid algorithm for flow at all speeds. *AIAA J*. 1992;30(11):2660–2669.
4. Demirdzic I, Lilek Z, Peric M. A collocated finite volume method for predicting flows at all speeds. *Int J Numer Methods Fluids*. 1993;16(12):1029–1050.
5. Lien FS, Leschziner MA. A pressure-velocity solution strategy for compressible flow and its application to shock boundary-layer interaction using second-moment turbulence closure. *J Fluids Eng*. 1993;115(4):717–725.
6. Marchi CH, Maliska CR. A nonorthogonal finite-volume method for the solution of all speed flows using co-located variables. *Numer Heat Transf B*. 1994;26(3):293–311.
7. Yang HQ, Habchi SD, Przekwas AJ. General strong conservation formulation of Navier-stokes equations in nonorthogonal curvilinear coordinates. *AIAA J*. 1994;32(5):936–941.
8. Politis ES, Giannakoglou KC. A pressure-based algorithm for high-speed turbomachinery flows. *Int J Numer Methods Fluids*. 1997;25(1):63–80.
9. Lien FS, Leschziner MA. A general non-orthogonal collocated finite volume algorithm for turbulent flow at all speeds incorporating second-moment turbulence-transport closure, Part 2: application. *Comput Methods Appl Mech Eng*. 1994;114(1-2):149–167.
10. Shyy W, Thakur S. Controlled variation scheme in a sequential solver for recirculating flows. *Heat Transf*. 1994;25(3):245–272.
11. Karimian SMH, Schneider GE. Pressure-based control-volume finite element method for flow at all speeds. *AIAA J*. 1995;33(9):1611–1618.
12. Kobayashi MH, Pereiraf JCE. Characteristic-based pressure correction at all speeds. *AIAA J*. 1996;34(2):272–280.
13. Thukur S, Wright J, Shyy W, Liu J, Ouyang H, Vu T. Development of pressure-based composite multigrid methods for complex fluid flows. *Prog Aerosp Sci*. 1996;32(4):313–375.
14. Issa RI, Javareshkian MH. Application of TVD schemes in pressure-based finite-volume methods. In The 1996 ASME Fluids Engineering Division Summer Meeting. Part 3(of 3). San Diego, CA; 07/07-11/96. 1996;159-164.
15. Issa RI, Javareshkian MH. Pressure-based compressible calculation method utilizing total variation diminishing schemes. *AIAA J*. 1998;36(9):1652–1657.
16. Djavareshkian MH, Reza-zadeh S. Application of normalized flux in pressure-based algorithm. *Comput Fluids*. 2007;36(7):1224–1234.
17. Moukalled F, Darwish M. A high-resolution pressure-based algorithm for fluid flow at all speeds. *J Comput Phys*. 2001;168(1):101–130.
18. van der Heul DR, Vuik& C, Wesseling P. A conservative pressure-correction method for flow at all speeds. *Comput Fluids*. 2003;32(8):1113–1132.
19. Darwish M, Sraj& I, Moukalled F. A coupled finite volume solver for the solution of incompressible flows on unstructured grids. *J Comput Phys*. 2009;228(1):180–201.

20. Chen Z, Przekwas AJ. A coupled pressure-based computational method for incompressible/compressible flows. *J Comput Phys*. 2010;229(24):9150–9165.
21. Darwish& M, Moukalled F, fully coupled A. Navier–Stokes solver for fluid flow at all speeds. *Numer Heat Transf B Fund*. 2014;65(5):410–444.
22. Xiao CN, Denner F, van Wachem BG. Fully-coupled pressure-based finite-volume framework for the simulation of fluid flows at all speeds in complex geometries. *J Comput Phys*. 2017;346:91–130.
23. Sidilkover D. Towards unification of the vorticity confinement and shock capturing (TVD and ENO/WENO) methods. *J Comput Phys*. 2017;358:235-255. https://doi.org/10.1016/j.jcp.2017.12.033.
24. Wong ML, Lele SK. High-order localized dissipation weighted compact nonlinear scheme for shock and interface-capturing in compressible flows. *J Comput Phys*. 2017;339:179-209. https://doi.org/10.1016/j.jcp.2017.03.008.
25. Niu Y-Y. Computations of two-fluid models based on a simple and robust hybrid primitive variable Riemann solver with AUSMD. *J Comput Phys*. 2015;308:389-410. https://doi.org/10.1016/j.jcp.2015.12.045.
26. Kitamura K. Assessment of SLAU2 and other flux functions with slope limiters in hypersonic shock-interaction heating. *Comput Fluids*. 2016;129:134–145.
27. Fu L, Hu XY, Adams NA. A new class of adaptive high-order targeted ENO schemes for hyperbolic conservation laws. *J Comput Phys*. 2018;374:724-751. https://doi.org/10.1016/j.jcp.2018.07.043.
28. Xu W, Wu W. Improvement of third-order WENO-Z scheme at critical points. *Comput Math Appl*. 2018;75:3431-3452. https://doi.org/10.1016/j.camwa.2018.02.009.
29. Huang C, Chen LL. A new adaptively central-upwind sixth-order WENO scheme. *J Comput Phys*. 2017;357:1-15. https://doi.org/10.1016/j.jcp.2017.12.032.
30. Wang B, Xiang G, Xiangyu YH. An incremental-stencil WENO reconstruction for simulation of compressible two-phase flows. *Int J Multiphase Flow*. 2018;104:20–31. https://doi.org/10.1016/j.ijmultiphase%C3%9Fow.2018.03.013.
31. Peng J, ChuanleiZhai GN, Yong H, Shen Y. An Adaptive characteristic-wise reconstruction WENO-Z scheme for gas dynamic Euler equations. *Comput Fluids*. 2019;179:34–51. https://doi.org/10.1016/j.comp%C3%9Fuid.2018.08.008.
32. Wang B-S, Li P, Gao Z, Don WS. An improved fifth order alternative WENO-Z finite difference scheme for hyperbolic conservation laws. *J Comput Phys*. 2018;374:469-477. https://doi.org/10.1016/j.jcp.2018.07.052.
33. Chai D, Xi G, Sun Z, Wang Z, Huang Z. An efficient modified WENO scheme based on the identification of infection points. *Comput Fluids*. 2018;170:176–186. https://doi.org/10.1016/j.comp%C3%9Fuid.2018.04.036.
34. Cravero I, Puppo G, Semplice M, Visconti G. Cool WENO schemes. *Comput Fluids*. 2018;169:71–86.
35. Harten A, Osher S. Uniformly high-order accurate nonoscillatory schemes I. *Siam J Numer Anal*. 1986;24(2):279–309.
36. Harten A, Osher S, Engquist B, Chakravarthy SR. Some results on uniformly high-order accurate essentially nonoscillatory schemes. *Appl Numer Math*. 1986;2(3-5):347–377.
37. Harten A, Osher S, Engquist B, Chakravarthy SR. Uniformly high order accurate essentially non-oscillatory schemes, III. *J Comput Phys*. 1997;131(1):3–47.
38. Harten A. ENO schemes with subcell resolution. *J Comput Phys*. 1989;83(1):148–184.
39. Liu XX-D, Osher S, Chan T. Weighted essentially non-oscillatory schemes. *J Comput Phys*. 1994;115(1):200–212.
40. Jiang GS, Shu CW. Efficient implementation of weighted ENO schemes. *J Comput Phys*. 1996;126(1):202–228.
41. Henrick AK, Aslam TD, Powers JM. Mapped weighted essentially non-oscillatory schemes: achieving optimal order near critical points. *J Comput Phys*. 2005;207(2):542–567.
42. Borges R, Carmona M, Costa B, Don WS. An improved weighted essentially non-oscillatory scheme for hyperbolic conservation laws. *J Comput Phys*. 2008;227(6):3191–3211.
43. Gerolymos GA, Sénéchal D, Vallet I. Very-high-order WENO schemes. *J Comput Phys*. 2009;228(3):8481–8524.
44. Zhao S, Lardjane N, Fedioun I. Comparison of improved finite-difference WENO schemes for the implicit large eddy simulation of turbulent non-reacting and reacting high-speed shear flows. *Comput Fluids*. 2014;95:74–87.
45. Tao Z, Li F, Qiu J. High-order central Hermite WENO schemes on staggered meshes for hyperbolic conservation laws. *J Comput Phys*. 2015;281:148–176.
46. Chorin AJ. A numerical method for solving incompressible viscous flow problems. *J Comput Phys*. 1997;135(2):118–125.
47. E. Turkel, A. Fiterman, B. van Leer, *Preconditioning and the Limit to the Incompressible Flow Equations, Technical Report, NASA-Cr-191500*, Hampton, VA: Institute for Computer Applications in Science and Engineering; 1993.
48. Cubero& A, Fueyo N. Preconditioning based on a partially implicit implementation of momentum interpolation for coupled solvers. *Numer Heat Transf B Fund*. 2008;53(6):510–535.
49. Hejranfar K, Kamali-Moghadam R. Preconditioned characteristic boundary conditions for solution of the preconditioned Euler equations at low Mach number flows. *J Comput Phys*. 2012;231(12):4384–4402.
50. Hejranfar K, Parseh K. Application of a preconditioned high-order accurate artificial compressibility-based incompressible flow solver in wide range of Reynolds numbers. *Int J Numer Methods Fluids*. 2018;86(1):46–77.
51. Hejranfar K, Parseh K. Preconditioned characteristic boundary conditions based on artificial compressibility method for solution of incompressible flows. *J Comput Phys*. 2017;345:543–564. https://doi.org/10.1016/j.jcp.2017.05.014.
52. Wesseling P. *Principles of Computational Fluid Dynamics*. 29. New York, NY: Springer Science & Business Media; 2009.
53. San O, Kara K. Numerical assessments of high-order accurate shock capturing schemes: Kelvin–Helmholtz type vortical structures in high-resolutions. *J Comput Fluids*. 2014;89:254–286.

54. Hirsch C. *Numerical Computation of Internal and External Flows, Vol. 2-Computational Methods for Inviscid and Viscous Flows*. New York, NY: Chichester; 1990.
55. Issa RI. Solution of implicit discretised fluid flow equations by operator splitting. *J Comput Phys*. 1986;62(1):40–65.
56. Anderson JD. *Modern Compressible Flow with Historical Perspective*. 3rd ed. New York, NY: McGraw-Hill Education; 2003.
57. Lax PD, Liu XD. Solution of two-dimensional Riemann problems of gas dynamics by positive schemes. *SIAM J Sci Comput*. 1998;19(2):319–340.
58. Uslu S. *Numerical Prediction of Transonic Flow in Turbine Blade Passages* [thesis]; Submitted for Degree of Doctor of Philosophy, University of London, Imperial College; 1993.

How to cite this article: Balaj M, Djavareshkian MH. Implementation of weighted essentially non-oscillatory scheme for unsteady and steady compressible flow in pressure-based algorithm. *Int J Numer Meth Fluids*. 2021;93:2249–2271. https://doi.org/10.1002/fld.4972